Journal of Materials Chemistry A

PAPER

View Article Online
View Journal | View Issue

Cite this: J. Mater. Chem. A, 2016, 4, 12434

Preparation of porous MoO_2@C nano-octahedrons from a polyoxometalate-based metal–organic framework for highly reversible lithium storage†

Guoliang Xia,[a] Dong Liu,[a] Fangcai Zheng,[a] Yang Yang,[a] Jianwei Su[a] and Qianwang Chen*[ab]

Received 26th April 2016
Accepted 6th July 2016

DOI: 10.1039/c6ta03491h

www.rsc.org/MaterialsA

Molybdenum oxide has been investigated as a host material for lithium-ion batteries due to its high theoretical capacity (838 mA h g^{-1}), low electrical resistivity, high stability and high electrochemical activity toward lithium. However, a dramatic volume expansion occurred during the charge/discharge process, which results in anode pulverization and thereafter a rapid capacity fading and limits its application as an anode material. Herein, we report the preparation of MoO_2 nanoparticles embedded in a porous octahedral carbon matrix (denoted as MoO_2@C) by using a polyoxometalate-based metal–organic framework (PMOF) as the precursor. This facile strategy ensures the *in situ* formation of a porous carbon matrix which could increase active sites to store redox ions and enhance the ionic diffusivity of the encapsulated MoO_2 nanoparticles. Benefiting from such unique structures, the MoO_2@C composite is capable of delivering a high reversible specific capacity of 1442 mA h g^{-1} after 50 cycles at a current density of 100 mA g^{-1} and 443.8 mA h g^{-1} after 850 cycles at a current density of 1000 mA g^{-1} as an anode material.

Introduction

Rechargeable lithium-ion batteries (LIBs) as important power sources have been intensively pursued in recent years.[1] The superiorities such as large capacity, long longevity, high energy density and low self-discharge make LIBs the best system for upcoming mobile electric devices and hybrid electric vehicles.[2] Commercialized graphite has been widely used as the anode material in LIBs; however it has a limited theoretical capacity of around 372 mA h g^{-1} due to the formation of the intercalation compound LiC_6. On the other hand, traditional lithium-storage materials suffer from serious capacity loss as a result of the high polarization and sluggish diffusion of Li^+ ions and electrons in the electrode materials, when discharged and charged at high rates. To improve the performance of LIBs, great efforts have been focused to develop new electrode materials, design novel electrode structures, and decrease inactive ingredients in the electrodes. Different advanced materials are mushrooming to substitute traditional electrode materials, offering great potential for next generation high power and energy LIBs. Among these available anode materials, metal oxides,[3] such as Fe_2O_3,[4,5] SnO_2,[6] Co_3O_4,[7] MnO,[8] NiO,[9] CuO,[10] TiO_2,[11] and MoO_2,[12] have been regarded as very appealing candidates, because of their high capacity, wide-spread availability, enhanced safety and low cost. However, their remarkable lithium-storage capacities are usually accompanied by the inherent poor electrical conductivity and large volume change upon cycling, resulting in rapid decay in capacity and limited rate performance. Therefore, fabricating high performance metal-oxide electrode materials with both large reversible capacity and long cycle time still remains a big challenge.

Benefiting from a high surface area and short diffusion distance for lithium ions or electrons, nanostructured materials exhibit superior performance.[13] In particular, hierarchically or hollow nanostructured materials[14] have attracted great attention owing to their extraordinary features of large surface areas, robust stability, distinct interior voids, low density and decreased transport distance for both mass and charge transport. Moreover, carbon has been used as a buffer to protect the electrode materials as well as improve the electrical conductivity. Based on these strategies, so many inspiring studies have been reported. Huang *et al.* synthesized hierarchical mesoporous urchin-like Mn_3O_4/carbon microspheres and this material showed a high lithium storage capacity of 915 mA h g^{-1} at 100 mA g^{-1} after 50 cycles, great cycling stability and excellent rate capability.[15] Zou *et al.* reported that the carbon-stabilized ZnO/$ZnFe_2O_4$ uniform porous hollow octahedral

[a]Hefei National Laboratory for Physical Science at Microscale, Department of Materials Science & Engineering, Collaborative Innovation Center of Suzhou Nano Science and Technology, University of Science and Technology of China, Hefei 230026, China. E-mail: cqw@ustc.edu.cn

[b]High Magnetic Field Laboratory, Hefei Institutes of Physical Science, Chinese Academy of Sciences, Hefei 230031, China

† Electronic supplementary information (ESI) available. See DOI: 10.1039/c6ta03491h

nanoparticle electrode material reaches a capacity of 1390 mA h g^{-1} over 100 cycles at a current density of 100 mA g^{-1}, and even at 2 A g^{-1}, after 100 cycles, delivers a capacity of 988 mA h g^{-1}.[16]

Molybdenum oxide has attracted attention as a host material owing to its excellent electrochemical characteristics. In particular, it has a high theoretical capacity (838 mA h g^{-1}), low electrical resistivity, high stability, and high electrochemical activity toward lithium. However, the application of MoO_2 as an anode material failed to meet expectations due to rapid capacity fading resulting from phase transformation and dramatic volume change during lithiation and delithiation, which leads to breakdown of electrical pathways.[17] As a consequence, thoughtful efforts have been focused on searching for MoO_2-based electrical materials with unique structures to solve the inherent poor electrical conductivity and significant volume change. One of the effective approaches is to coat or hybridize MoO_2 materials with advanced carbon materials, which can enhance power and energy densities and improve the cycling performance.[18–20] Carbon materials can greatly enhance the electrical conductivity of MoO_2, and effectively relieve the strain caused by the volumetric change, as a specified buffer. These strategies have been demonstrated for the synthesis of uniform carbon-coated MoO_2 nanospheres[18] and nanofibers,[21] MoO_2/carbon hybrid nanowires,[20] and MoO_2 nanoparticles attached on graphene.[19,22] For example, Huang *et al.* synthesized 3D graphene supported MoO_2 through a facile chemical vapor deposition (CVD), and it delivered high reversible capacities of 975.4 mA h g^{-1} and 537.3 mA h g^{-1} at a current density of 50 and 1000 mA g^{-1}.[22] Tang *et al.*[12] reported that a hybrid consisting of reduced graphene oxide (rGo) sheet-wrapped MoO_2 porous nanobelts had a high reversible capacity (974 mA h g^{-1} charging capacity at 60 mA g^{-1}). And this rGo wrapping layers stabilize the nanophase transition in MoO_2 and alleviate volume swing effects during the lithiation/delithiation process. However, the synthesis of MoO_2-based nanostructures and nanocomposites usually involves tedious and complicated processes, and time-consuming hydrothermal synthesis in autoclaves, such as CVD and preparation of graphene oxide[23] and nanostructured MoO_2 particles.

In recent years, metal–organic frameworks have attracted extensive research interest in virtue of their porosity and tunable functionalities, as well as widespread applications in catalysis,[24] and electrochemical energy storage and conversion.[25,26] On the other hand, syntheses of functional materials from MOFs have caught special interest. In particular, inspired by their high surface area, porosities, and abundant carbon-containing organic linkers, MOFs have been considered as promising precursors and templates to fabricate porous carbon, metal oxide, metal/carbon and metal oxide/carbon nanostructured materials. Xu *et al.*[27] first employed MOF-5 as a template to prepare nanoporous carbon, which provided a new example of application of the rapidly growing MOF family. By engineering the MOF precursor or calcination conditions, the structure and composition of MOF-derived nanomaterials can be tuned and optimized to achieve excellent anode performances for LIBs. Also, it is widely believed that hollow metal oxide nanostructures could provide a higher capacity and better stability. The Kirkendall effect was explored to obtain porous Co_3O_4 nanocages from the Prussian blue analogue, $Co_3[Co(CN)_6]_2$, by calcination at 400 °C in air.[28] Lou *et al.* first put forward that starting with metal–organic frameworks, the large-scale and facile synthesis of complex hollow microboxes can be available *via* manipulation of template-engaged reactions between the Prussian blue template and different alkaline substances, and these microboxes exhibit remarkable electrochemical performance as anode materials for lithium-ion batteries.[29] Zheng *et al.* reported nitrogen-doped graphene particle analogues by using a nitrogen-containing zeolitic imidazolate framework (ZIF-8) as a precursor.[30] And metal oxides embedded in the carbon matrix can be synthesized by the calcination of oxygen-containing MOFs under a N_2 atmosphere or oxygen-free MOFs in oxygen. Zheng *et al.* also synthesized MnO nanoparticles distributed in the porous carbon matrix by annealing Mn-based metal–organic frameworks which consist of Mn^{2+} ions and oxygen-containing trimesic acid linkers under an inert N_2 atmosphere.[31] The CoO nanoparticles embedded in a nitrogen-rich graphitic carbon matrix can be synthesized by thermal decomposition of oxygen-free metal–organic framework ZIF-67 under a flow of Ar and air.[32] Obviously a high content of carbon or heteroatoms in MOF-derived metal oxide nanostructures should be desired for a significantly enhanced anode performance. In this regard, it is of importance to synthesize porous nano-structures consisting of both metal oxide nanoparticles and abundant carbon through a one-step calcination of a MOF precursor.

Polyoxometalate-based metal–organic frameworks (POMOFs) have attracted special interest for potential applications in catalysis due to their high thermal stability, porous structure, extra chemical composition, high specific surface area, and versatile organic fragments.[33–35] However, there are few reports on using POMOF as a precursor to prepare a new lithium-ion battery anode material. In this work, we developed a facile and scalable *in situ* synthesis strategy to fabricate MoO_2 nanoparticles homogeneously distributed in the porous carbon matrix (denoted as MoO_2@C) by annealing ambient-temperature prepared polyoxometalate-based metal–organic frameworks (NENU-5) which contain Mo-based POM units and metal–organic frameworks forming intriguing structures.[36] The Mo-based POM units and metal–organic frameworks were phosphomolybdic acid hydrate and Cu-based MOFs, respectively. Distinct from previous studies, the present synthesis strategy relies on an *in situ* and enclosed carburization reaction between the oxygen-containing trimesic acid linkers and polyoxometalates that reside in the pores of the MOF host. This strategy is easy, tunable, and cost-effective, and therefore it is highly promising for mass production.

Experimental section and methods

Material preparation

All chemicals are of analytical grade, and were used without any further purification. The octahedral POMOF (NENU-5) precursor was synthesized according to the previous research.[35] The typical procedure is as follows. Solution A: 1 mmol copper(II) acetate monohydrate, 1 mmol L-glutamic acid, and 0.3 g

of phosphomolybdic acid hydrate were dissolved in a deionized water (40 ml) system under agitated stirring for nearly 20 minutes to get a transparent solution. Solution B: 0.67 mmol of 1,3,5-benzenetricarboxylic acid was completely dissolved under ultrasonic conditions in 40 ml of ethanol. Then solution B was poured into solution A with continuous stirring and a deep green precipitate (NENU-5 nanocrystals) appeared immediately. During the reaction, these non-coordinating POM units could be distributed homogeneously in the solution and surrounded by organic ligands in the atomic scale, therefore guaranteeing an *in situ* and consistent carburization reaction that can effectively prevent generated MoO_2 nanoparticles from agglomeration. After stirring for 14 h, the precipitate was collected by centrifugation and washed several times with absolute ethanol and dried in an oven at 60 °C for further use. The Cu–MoO_2@C nano-octahedrons were successfully obtained by thermal decomposition of the as-prepared precursor at 600 °C for 5 h with a temperate ramp rate of 5 °C min^{-1} under a N_2 atmosphere. After that, the copper particles were removed by dispersing the annealed sample in 0.1 M $FeCl_3$ aqueous solution with strong stirring for 2 h. The resulting porous MoO_2@C nano-octahedrons were collected by centrifugation with deionized water repeatedly and absolute ethanol, and finally dried at 60 °C overnight. Similarly, the carbon matrix was synthesized through the same method without the addition of phosphomolybdic acid hydrate.

Material characterization

The powder X-ray diffraction (XRD) patterns of all samples were recorded with an X-ray diffractometer (Japan Rigaku D/MAX-γA) equipped with Cu-Kα radiation ($\lambda = 1.54178$ Å) over the 2θ range of 20–80°. Field emission scanning electron microscopy (FE-SEM) images were collected on a JEOL JSM-6700 M scanning electron microscope. Transmission electron microscopy (TEM) images were taken on a Hitachi H-800 transmission electron microscope using an accelerating voltage of 200 kV, and a high-resolution transmission electron microscope (HRTEM) (jeol-2011) was operated at an acceleration voltage of 200 kV. The specific surface area was evaluated at 77 K (Micromeritics ASAP 2020) using the Brunauer–Emmett–Teller (BET) method, while the pore volume and pore size were calculated according to the Barrett–Joyner–Halenda (BJH) formula applied to the adsorption branch. Thermogravimetric analysis (TGA) was carried out using a Shimadzu-50 thermoanalyser under nitrogen flow. XPS measurements were performed on a VGESCALAB MKIIX-ray photoelectron spectrometer with an $Mg_{k\alpha}$ excitation source (1253.6 eV).

Electrochemical measurements

The electrochemical behavior of the porous MoO_2@C was evaluated using CR2032 coin-type cells with lithium serving as the counter electrode and the reference electrode. To prepare a working electrode, the as-synthesized active material (MoO_2@C, 80 wt%), conductive material (acetylene black, 10 wt%), and the polymer binder (PVDF, 10 wt%) were mixed in *N*-methyl-2-pyrrolidone. The mixture was subsequently brush coated on copper foil and then dried at 80 °C for 12 h. The electrolyte used in the cells was 1.00 M $LiPF_6$ in ethylene carbonate and diethyl carbonate (EC/DEC = 1 : 1). The cells were assembled in an argon-filled glovebox with both the moisture and the oxygen contents below 1 ppm (Mikrouna, Super (1220/750/900)). Cyclic voltammograms (CV) were obtained on a CHI760E electrochemical workstation. The electrode capacity was measured using the galvanostatic discharge/charge method and employing a battery test system (Neware CT-3008W) with a voltage range between 0.01 and 3.0 V.

Results and discussion

As illustrated in Scheme 1, the as-prepared NENU-5 nano-octahedrons were calcined at 600 °C for 5 h under a N_2

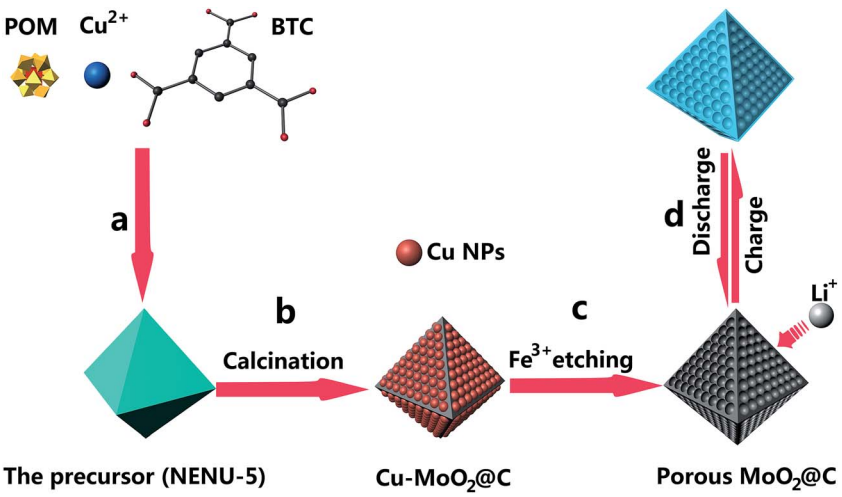

Scheme 1 Schematic illustration of the synthesis procedure for the porous MoO_2@C nano-octahedrons. (a) Synthesis of the NENU-5 precursor at ambient temperature. (b) Formation of Cu–MoO_2@C nano-octahedrons after annealing at 600 °C for 5 h under a N_2 atmosphere. (c) Removal of metallic Cu nanoparticles by Fe^{3+} etching to produce porous MoO_2@C nano-octahedrons. (d) The resulting porous MoO_2@C nano-octahedrons serve as electrochemical reactors for LIBs.

atmosphere. During the annealing process, the MoO_2 nanoparticles would be formed through the decomposition of Mo-based POM. Meanwhile, the Cu^{2+} clusters were reduced to metallic Cu and a carbon skeleton came into being from BTC ligands. Finally, MoO_2@C nano-octahedrons were obtained after removing metallic Cu with an aqueous solution of $FeCl_3$, which was confirmed by XRD analysis (see ESI, Fig. S1†), and then used as an anode material for lithium-ion batteries.

A field-emission scanning electron microscopy (FESEM) image of NENU-5 particles is shown in Fig. 1a. Clearly, the precursor particles with a diameter of approximately ~1 μm show a good uniformity, which can also be seen from the transmission electron microscopy (TEM) image (see ESI, Fig. S2†). Besides, the XRD pattern of the as-synthesized NENU-5 (see ESI, Fig. S3†) matches well with that of simulated NENU-5, and confirms the phase purity and good crystallinity.[37] The TGA-DSC curves of NENU-5 under a N_2 atmosphere are displayed in Fig. 1b. It is found that the NENU-5 precursor underwent a significant weight loss of 19.47% from room temperature to 147 °C, indicating the loss of H_2O molecules from the porous structure. When the degradation temperature was further increased to 443 °C, a weight loss of 29.12% was observed between 147 °C and 443 °C due to the composition of metal–organic frameworks as well as PMo_{12}; meanwhile, MoO_3 formed. As the temperature increased, oxygen molecules were removed by combining with the pyrolysis carbon and phosphorous; at the same time, Mo(VI) turned into Mo(IV) and MoO_3 reduced to MoO_2 which is relatively stable at high temperatures. However, as the carbonization temperature as well as time increased, for example, molybdenum carbide would be formed at 800 °C for 5 h.[35] Therefore, we managed to obtain MoO_2 nanoparticles embedded in the porous carbon matrix by keeping the carbonization temperature at 600 °C for 5 h.

After thermal decomposition and thereafter etching treatment, the porous MoO_2@C nano-octahedrons were investigated by FESEM and TEM. A FESEM (Fig. 2a) micrograph states clearly that the morphology of the precursor is well maintained, and the rough surface (see ESI, Fig. S4†) comes into being with the release of gaseous molecules, such as CO_2 and H_2O, during the thermal treatment. Fig. 2b displays a typical TEM image of porous MoO_2@C nano-octahedrons, and the sharp contrast indicates that ultrafine MoO_2 nanoparticles are homogeneously distributed in the porous carbon skeleton.

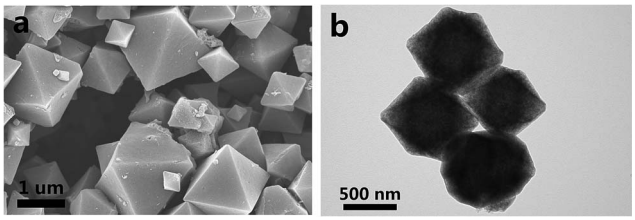

Fig. 2 (a, b) FESEM and TEM images of the as-made MoO_2@C nano-octahedrons.

The phase, chemical composition and local structure information of the products can be revealed by X-ray diffraction (XRD), Raman spectroscopy, and X-ray photoelectron spectroscopy (XPS). Fig. 3a shows the XRD pattern of the as-prepared MoO_2@C nano-octahedrons. It appears different from the pattern of the MoO_2 in the standard card due to the peak broadening effect aroused by small-size grains. Nevertheless, the main diffraction peaks can be indexed to the monoclinic MoO_2 phase (JPCDS card no. 32-0671). The broadened diffraction peaks indicate the nano-crystalline characteristics of MoO_2, which is uniformly distributed in the porous octahedral carbon matrix. Fig. 3b shows the Raman spectrum of MoO_2@C nano-octahedrons. The two obvious peaks at around 1352 and 1580 cm^{-1} were observed, corresponding to the disordered carbon (D-band) and the ordered graphitic carbon (G-band), respectively. Alternatively, the intensity of the G-band is obviously stronger than that of the D-band, which suggests a high degree of graphitization of the carbon in the products. This would be favorable to improve the electrical conductivity of the as-prepared sample. Besides, the survey spectrum of MoO_2@C demonstrates the existence of C, Mo and O elements (see ESI, Fig. S5a†).

The texture and porosity of the as-made sample were quantified by measuring the nitrogen adsorption isotherm at 77 K (Fig. 3c). It exhibits typical type-IV features of absorbents with a H2 hysteresis loop. According to the Brunauer–Emmett–Teller (BET) method, the specific surface area was estimated to be 485 $m^2 g^{-1}$, which is higher than those of previously reported hybrid structures of MoO_2 and carbon (see ESI, Table S1†). And such a large specific surface area significantly facilitates the enhancement of the performance of LIBs. In addition, the pore size distribution curve (Fig. 3d) obtained using the Barrett–Joyner–Halenda (BJH)

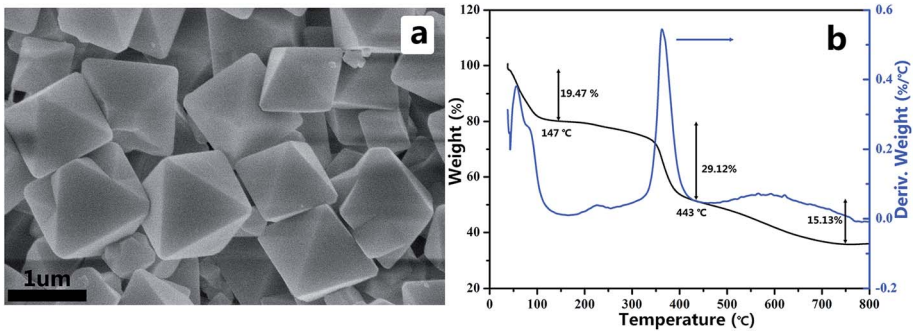

Fig. 1 (a) FESEM images of NENU-5 and (b) TGA-DSC curves of the NENU-5 in N_2.

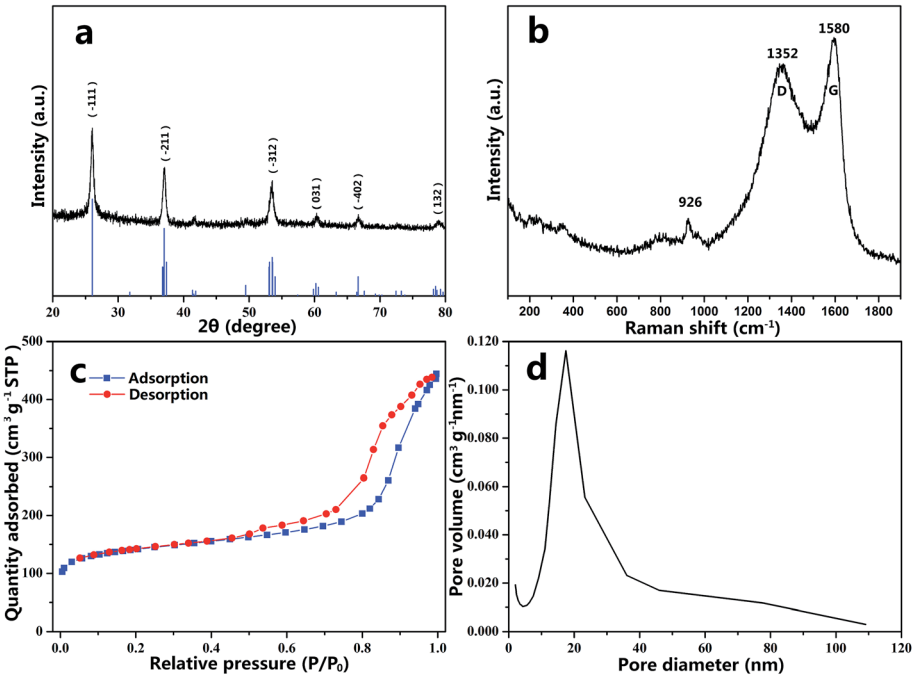

Fig. 3 (a) The XRD pattern, (b) Raman spectrum, (c) nitrogen adsorption isotherm at 77 K, and (d) the pore size distribution calculated using the BJH equation from N_2 adsorption.

method indicates a mesopore distribution concentrated at approximately 20 nm and an average pore size of 5.3 nm. On the basis of previous studies, a pore size of 2–10 nm facilitates rapid electrolyte transfer because the nanopores and interconnections provide more favorable pathways for ion penetration and transport.[26] Therefore, the as-prepared porous MoO_2@C nano-octahedrons are suggested to be an excellent anode material for LIBs.

The high-resolution TEM (HRTEM) image (Fig. 4a) taken from the edge of the MoO_2@C further demonstrates that MoO_2 particles are well-dispersed in the porous carbon matrix (see ESI, Fig. S6†). An obvious boundary of carbon labeled by an ellipse indicates that the whole MoO_2@C nano-octahedrons are wrapped by a thin carbon layer with an average size of 12 nm.

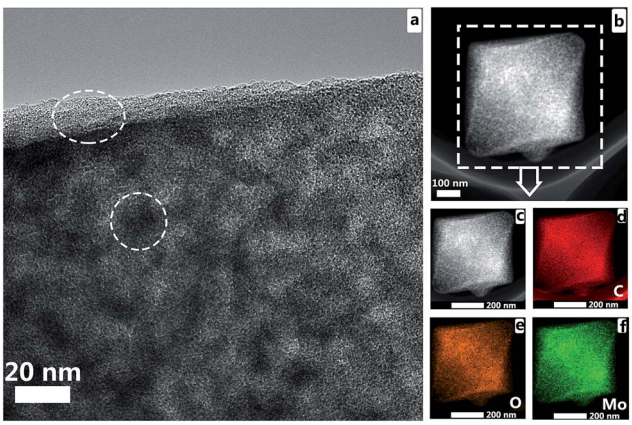

Fig. 4 (a–c) HRTEM images and (d–f) EDS mapping of MoO_2@C nano-octahedrons.

This *in situ* formed carbon layer not only enhanced the conductivity but also buffered the large volume variation during the Li^+ insertion and extraction process which leads to significant improvement in the cycling stability. Moreover, the MoO_2 nanoparticles labeled by a circle are distributed uniformly in the carbon matrix. A lattice spacing of 0.34 nm was measured and is shown in Fig. S7 (see ESI†), which is consistent with the *d* spacing of the (−111) planes of MoO_2. Fig. 4d–f further give typical TEM energy dispersive spectrometry (EDS) elemental mapping images of a single MoO_2@C nano-octahedron, evidently revealing the extremely homogeneous distribution of C, O and Mo species in the whole MoO_2@C nano-octahedron.

The electrochemical performances of the porous MoO_2@C nano-octahedrons have been evaluated in lithium half-cells. Fig. 5a shows the first three cyclic voltammetry (CV) curves of MoO_2@C at room temperature between 0.0 and 3.0 V at a scan rate of 0.1 mV s^{-1}. In the first cathodic polarization process, a weak reduction peak at approximately 1.16 V was observed probably as a result of the phase transition from the orthorhombic phase to the monoclinic phase upon lithium insertion.[38] A wide peak at around 0.6 V can be attributed to the irreversible reduction of the electrolyte and the formation of a solid electrolyte interface (SEI) layer. A wide oxidation peak at around 1.36 V and a sharp peak at 1.56 V were observed. In the next two cycles, only a pronounced pair of reduction and oxidation peaks (1.13/1.40 V) was found from the overlapping curves. Different from the reports of Zhou *et al.*,[39] the peaks were wide and not sharp, which may be attributed to the role of the carbon matrix.[31]

The cycling performance of the as-made MoO_2@C anode materials at a current density of 100 mA g^{-1} is presented in

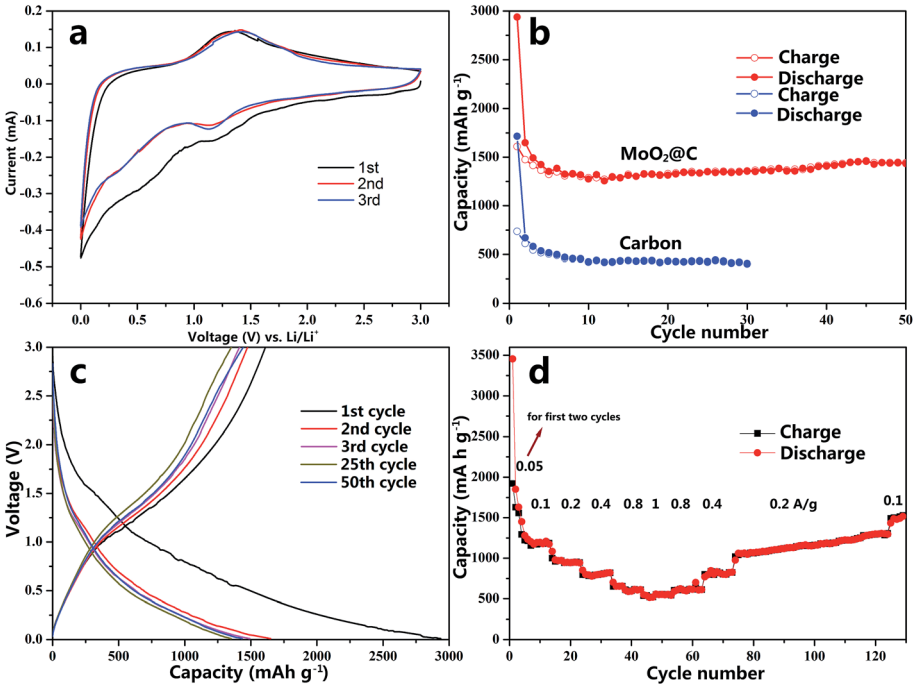

Fig. 5 (a) Cyclic voltammetry measurements on MoO_2@C during the first three cycles. The voltage range was from 0.0 to 3.0 at a scan rate of 0.1 mV s^{-1}. (b) Cycle-life performance of MoO_2@C and carbon matrix. (c) Discharge–charge curves of MoO_2@C. The cell was tested for 50 cycles between 0.1 mV and 3.0 V at a density of 100 mA g^{-1}. (d) Rate capability test for the MoO_2@C at various current densities (100–1000 mA g^{-1}).

Fig. 5b. After 5 cycles, the sample displays a stable cycling performance up to 50 cycles. And 1442 mA h g^{-1} was retained after 50 cycles. Even at a current density of 1 A g^{-1}, the as-prepared MoO_2@C electrode material shows excellent cycling stability and 443.8 mA h g^{-1} was held after 850 cycles (see ESI, Fig. S8†). We also tested the capacity of the carbon matrix which provided a reversible capacity of 402 mA h g^{-1} after 30 cycles at a current density of 100 mA g^{-1}. Fig. 5c displays the representative galvanostatic charge/discharge curves of MoO_2@C within a cutoff window of 0.01–3.0 V at a current density of 100 mA g^{-1}. The first discharge and charge capacities of the MoO_2@C electrode are 2936.8 and 1610.1 mA h g^{-1}, respectively, giving an initial coulombic efficiency of 54.8% (see ESI, Fig. S9†). The relatively low initial coulombic efficiency can be attributed to the irreversible capacity loss, including the formation of SEI films and decomposition of the electrolyte, which is common to most of the anode materials. Besides, a large specific surface area could also result in a low initial coulombic efficiency.[40–43] In the next cycle, a discharge capacity of 1648.9 mA h g^{-1} was achieved, while the coulombic efficiency rapidly increased to 89.5%. After 10 cycles, nearly 100% coulombic efficiency was achieved, and held for the following cycles. As shown in Fig. 5d, the rate performance of MoO_2@C was tested by cycling the cell at various current densities. With the increase in current density from 50 to 100, 200, 400, 800, 1000, 800, 400, 200, and 100 mA g^{-1}, the capacity changed from 1450 to 1185.7, 945, 819, 611, 543, 613.2, 823.2, 1077.4, 1305.7 and 1489 mA h g^{-1}, respectively. Such excellent rate capacity and cycling performance imply the good structural stability and electrochemical reversibility of our porous MoO_2@C nano-octahedrons. Moreover, as listed in Table S2 in the ESI,† the specific capacity and cycling performance of our porous MoO_2@C nano-octahedrons are comparable or even superior to those of MoO_2/C composites. The excellent electrochemical performance of MoO_2@C nano-octahedrons can be attributed to their unique nanostructure.

Firstly, the small MoO_2 nanoparticles (about 14 nm in diameter) can provide a large surface area and numerous active sites, which facilitate the reversible electrochemical reaction of MoO_2 with Li and also increase the active sites for Li^+ storage.[44] Importantly, the large surface area of MoO_2 nanoparticles also enlarges the contact area with the electrolyte, which is conducive to rapid and extensive charge transfer between the electrodes and electrolyte.[45] Therefore, the specific capacity of porous MoO_2@C nano-octahedrons can be significantly improved. Also, the aggregation of porous MoO_2@C octahedrons could form 3D dimensional clusters which are similar to tunnel-like frameworks. According to our previous study,[30] the generated nanopores or tunnels could provide more active sites, thus leading to an extra lithium storage capacity.

Secondly, as revealed by HRTEM (Fig. 4a), MoO_2 nanoparticles are well dispersed in the carbon skeleton, which provides a buffer environment. And MoO_2 nanoparticles are well isolated from each other by the carbon matrix. Therefore, the aggregation of adjacent MoO_2 nanoparticles can be avoided. Since the cycling performance of MoO_2 nanoparticles depends strongly on the degree of aggregation, and like other transition-metal oxides, the aggregation of MoO_2 nanoparticles usually leads to irreversible deterioration in capacity.[46] In this regard, the isolation of MoO_2 nanoparticles by the carbon matrix also

contributes significantly to the excellent rate capacity and cycling stability. The SEM and TEM images of porous MoO_2@C nano-octahedrons after 50 cycles at a current density of 0.1 A g^{-1} and after 850 cycles at a current density of 1 A g^{-1} clearly show that the octahedral morphology could be well retained (see ESI, Fig. S11†). This observation proves the superior structural stability of porous MoO_2@C nano-octahedrons and indicates that the carbon matrix with good mechanical flexibility could provide sufficient space for large volumetric expansion during lithiation and delithiation processes.

In addition, the highly porous structure of the as-prepared MoO_2@C nano-octahedrons can provide more active sites for lithium ion storage. And adequate contact between the MoO_2@C electrode and electrolyte is ensured. The BJH pore size distribution curve (Fig. 3d) shows a broad range of size distribution and a mesopore distribution concentrated at approximately 20 nm. Such a mesoporous material facilitates rapid electrolyte transfer as nanopores and inter-connections provide more favorable pathways for ion penetration and transport.[26] Accordingly, the specific capacity and rate capability of porous MoO_2@C nano-octahedrons are enhanced. Moreover, the porous structures are capable of reducing the structure strain and buffering the large volume change during the Li^+ insertion and extraction process, thus leading to significant improvement in the cycling performance of MoO_2@C.[47]

Conclusion

In summary, we synthesized porous MoO_2@C nano-octahedrons consisting of MoO_2 nano-particles and carbon through direct calcination of the POMOF (NENU-5) precursor and thereafter etching treatment. The *in situ* generated carbon matrix provides an enhanced electrical conductivity and avoids the volume change during the discharge/charge process, which results in an excellent electrochemical performance. Benefiting from the unique structure and compositions, including MoO_2 nanoparticles, graphitic carbon matrix, and high porosity, the MoO_2@C nano-octahedrons exhibit excellent capacity and cycling stability (1442 mA h g^{-1} after 50 cycles at 100 mA g^{-1} and 443.8 mA h g^{-1} after 850 cycles at 1000 mA g^{-1}). These results demonstrate that such a kind of unique design is a successful combination of graphitic carbon and MoO_2 nanoparticles. In this regard, this strategy is also suitable to design and prepare metal oxide/carbon composite structures for application in high-performance LIBs and supercapacitors as well as catalysts.

Acknowledgements

This study was supported by the National Natural Science Foundation of China (NSFC, 21271163, U1232211, and 21571168), the CAS/SAFEA International Partnership Program for Creative Research Teams and CAS Hefei Science Center.

Notes and references

1 M. V. Reddy, G. V. Subba Rao and B. V. R. Chowdari, *Chem. Rev.*, 2013, **113**, 5364–5457.
2 Y. Tang, Y. Zhang, W. Li, B. Ma and X. Chen, *Chem. Soc. Rev.*, 2015, **44**, 5926–5940.
3 C. Yuan, H. B. Wu, Y. Xie and X. W. Lou, *Angew. Chem., Int. Ed.*, 2014, **53**, 1488–1504.
4 L. Zhang, H. B. Wu, S. Madhavi, H. H. Hng and X. W. Lou, *J. Am. Chem. Soc.*, 2012, **134**, 17388–17391.
5 F. Zheng, M. He, Y. Yang and Q. Chen, *Nanoscale*, 2015, **7**, 3410–3417.
6 L. Zhang, H. B. Wu, B. Liu and X. W. Lou, *Energy Environ. Sci.*, 2014, **7**, 1013–1017.
7 M. V. Reddy, G. Prithvi, K. P. Loh and B. V. R. Chowdari, *ACS Appl. Mater. Interfaces*, 2014, **6**, 680–690.
8 Y. Xia, Z. Xiao, X. Dou, H. Huang, X. Lu, R. Yan, Y. Gan, W. Zhu, J. Tu, W. Zhang and X. Tao, *ACS Nano*, 2013, **7**, 7083–7092.
9 X. Zheng, H. Wang, C. Wang, Z. Deng, L. Chen, Y. Li, T. Hasan and B.-L. Su, *Nano Energy*, 2016, **22**, 269–277.
10 R. Wu, X. Qian, F. Yu, H. Liu, K. Zhou, J. Wei and Y. Huang, *J. Mater. Chem. A*, 2013, **1**, 11126–11129.
11 G. Zhang, H. B. Wu, T. Song, U. Paik and X. W. Lou, *Angew. Chem., Int. Ed.*, 2014, **53**, 12590–12593.
12 W. Tang, C. X. Peng, C. T. Nai, J. Su, Y. P. Liu, M. V. V. Reddy, M. Lin and K. P. Loh, *Small*, 2015, **11**, 2446–2453.
13 P. G. Bruce, B. Scrosati and J.-M. Tarascon, *Angew. Chem., Int. Ed.*, 2008, **47**, 2930–2946.
14 X. W. Lou, L. A. Archer and Z. Yang, *Adv. Mater.*, 2008, **20**, 3987–4019.
15 S.-Z. Huang, Y. Cai, J. Jin, J. Liu, Y. Li, Y. Yu, H.-E. Wang, L.-H. Chen and B.-L. Su, *Nano Energy*, 2015, **12**, 833–844.
16 F. Zou, X. Hu, Z. Li, L. Qie, C. Hu, R. Zeng, Y. Jiang and Y. Huang, *Adv. Mater.*, 2014, **26**, 6622–6628.
17 J. H. Ku, Y. S. Jung, K. T. Lee, C. H. Kim and S. M. Oh, *J. Electrochem. Soc.*, 2009, **156**, A688–A693.
18 Z. Wang, J. S. Chen, T. Zhu, S. Madhavi and X. W. Lou, *Chem. Commun.*, 2010, **46**, 6906–6908.
19 Q. Tang, Z. Shan, L. Wang and X. Qin, *Electrochim. Acta*, 2012, **79**, 148–153.
20 Q. Gao, L. Yang, X. Lu, J. Mao, Y. Zhang, Y. Wu and Y. Tang, *J. Mater. Chem.*, 2010, **20**, 2807–2812.
21 W. Luo, X. Hu, Y. Sun and Y. Huang, *Phys. Chem. Chem. Phys.*, 2011, **13**, 16735–16740.
22 Z. X. Huang, Y. Wang, Y. G. Zhu, Y. Shi, J. I. Wong and H. Y. Yang, *Nanoscale*, 2014, **6**, 9839–9845.
23 W. S. Hummers and R. E. Offeman, *J. Am. Chem. Soc.*, 1958, **80**, 1339.
24 Y. Yang, Z. Lun, G. Xia, F. Zheng, M. He and Q. Chen, *Energy Environ. Sci.*, 2015, **8**, 3563–3571.
25 W. Xia, A. Mahmood, R. Zou and Q. Xu, *Energy Environ. Sci.*, 2015, **8**, 1837–1866.
26 L. Hu and Q. Chen, *Nanoscale*, 2014, **6**, 1236–1257.
27 B. Liu, H. Shioyama, T. Akita and Q. Xu, *J. Am. Chem. Soc.*, 2008, **130**, 5390–5391.
28 L. Hu, N. Yan, Q. Chen, P. Zhang, H. Zhong, X. Zheng, Y. Li and X. Hu, *Chem.–Eur. J.*, 2012, **18**, 8971–8977.
29 L. Zhang, H. B. Wu and X. W. Lou, *J. Am. Chem. Soc.*, 2013, **135**, 10664–10672.
30 F. Zheng, Y. Yang and Q. Chen, *Nat. Commun.*, 2014, **5**, 5261.

31 F. Zheng, G. Xia, Y. Yang and Q. Chen, *Nanoscale*, 2015, **7**, 9637–9645.
32 S. Wang, M. Chen, Y. Xie, Y. Fan, D. Wang, J.-J. Jiang, Y. Li, H. Grützmacher and C.-Y. Su, *Small*, 2016, **12**, 2365–2375.
33 J.-S. Qin, D.-Y. Du, W. Guan, X.-J. Bo, Y.-F. Li, L.-P. Guo, Z.-M. Su, Y.-Y. Wang, Y.-Q. Lan and H.-C. Zhou, *J. Am. Chem. Soc.*, 2015, **137**, 7169–7177.
34 Y.-J. Tang, M.-R. Gao, C.-H. Liu, S.-L. Li, H.-L. Jiang, Y.-Q. Lan, M. Han and S.-H. Yu, *Angew. Chem., Int. Ed.*, 2015, **54**, 12928–12932.
35 H. B. Wu, B. Y. Xia, L. Yu, X.-Y. Yu and X. W. Lou, *Nat. Commun.*, 2015, **6**, 6512.
36 D.-Y. Du, J.-S. Qin, S.-L. Li, Z.-M. Su and Y.-Q. Lan, *Chem. Soc. Rev.*, 2014, **43**, 4615–4632.
37 C.-Y. Sun, S.-X. Liu, D.-D. Liang, K.-Z. Shao, Y.-H. Ren and Z.-M. Su, *J. Am. Chem. Soc.*, 2009, **131**, 1883–1888.
38 B. Guo, X. Fang, B. Li, Y. Shi, C. Ouyang, Y.-S. Hu, Z. Wang, G. D. Stucky and L. Chen, *Chem. Mater.*, 2012, **24**, 457–463.
39 L. Zhou, H. B. Wu, Z. Wang and X. W. Lou, *ACS Appl. Mater. Interfaces*, 2011, **3**, 4853–4857.
40 E. Frackowiak, K. Metenier, V. Bertagna and F. Beguin, *Appl. Phys. Lett.*, 2000, **77**, 2421–2423.
41 K. Ui, D. Fujii, Y. Niwata, T. Karouji, Y. Shibata, Y. Kadoma, K. Shimada and N. Kumagai, *J. Power Sources*, 2014, **247**, 981–990.
42 K. Zaghib, G. Nadeau and K. Kinoshita, *J. Electrochem. Soc.*, 2000, **147**, 2110–2115.
43 M. Winter, P. Novák and A. Monnier, *J. Electrochem. Soc.*, 1998, **145**, 428–436.
44 J. Jamnik and J. Maier, *Phys. Chem. Chem. Phys.*, 2003, **5**, 5215–5220.
45 S. Goriparti, E. Miele, F. De Angelis, E. Di Fabrizio, R. Proietti Zaccaria and C. Capiglia, *J. Power Sources*, 2014, **257**, 421–443.
46 P. Poizot, S. Laruelle, S. Grugeon, L. Dupont and J. M. Tarascon, *Nature*, 2000, **407**, 496–499.
47 J.-K. Sun and Q. Xu, *Energy Environ. Sci.*, 2014, **7**, 2071–2100.